Article

Optical observation of single spins in silicon

https://doi.org/10.1038/s41586-022-04821-y

Received: 8 April 2021

Accepted: 28 April 2022

Published online: 13 July 2022

Check for updates

Daniel B. Higginbottom[1,4], Alexander T. K. Kurkjian[1,2,4], Camille Chartrand[1,2], Moein Kazemi[1], Nicholas A. Brunelle[1], Evan R. MacQuarrie[1,2], James R. Klein[1], Nicholas R. Lee-Hone[1,2], Jakub Stacho[1], Myles Ruether[1], Camille Bowness[1,2], Laurent Bergeron[1], Adam DeAbreu[1], Stephen R. Harrigan[1], Joshua Kanaganayagam[1], Danica W. Marsden[1], Timothy S. Richards[1], Leea A. Stott[1], Sjoerd Roorda[3], Kevin J. Morse[1,2], Michael L. W. Thewalt[1] & Stephanie Simmons[1,2]✉

The global quantum internet will require long-lived, telecommunications-band photon–matter interfaces manufactured at scale[1]. Preliminary quantum networks based on photon–matter interfaces that meet a subset of these demands are encouraging efforts to identify new high-performance alternatives[2]. Silicon is an ideal host for commercial-scale solid-state quantum technologies. It is already an advanced platform within the global integrated photonics and microelectronics industries, as well as host to record-setting long-lived spin qubits[3]. Despite the overwhelming potential of the silicon quantum platform, the optical detection of individually addressable photon–spin interfaces in silicon has remained elusive. In this work, we integrate individually addressable 'T centre' photon–spin qubits in silicon photonic structures and characterize their spin-dependent telecommunications-band optical transitions. These results unlock immediate opportunities to construct silicon-integrated, telecommunications-band quantum information networks.

A pinnacle achievement of modern quantum science has been to isolate, control and harness individual quantum particles such as single charges, single photons and single spins. Individual atomic centres in solids have been the basis of a wide variety of scientific breakthroughs, including entanglement generation[2,4,5], long-distance teleportation[6], a loophole-free Bell's inequality test[7] and memory-enhanced quantum communications[8]. Central to each of these achievements were 'photon–spin centres': solid-state centres possessing spin(s) and spin-dependent optical transitions. Such spins may be remotely entangled through photons to form quantum computing and communication networks[2]. Many more breakthroughs await photon–spin networks at scale.

A compelling approach to generating large entangled networks of photon–spin centres is through integrated photonics. Unfortunately, the most developed integrated photonics platforms, such as Si and InP, are not host materials to the most well-studied photon–spin centres, such as centres in YSO[9], YVO[10], hBN[11,12] and, most notably, diamond[2,4,6,7,13,14]. Efforts are underway to engineer integrated diamond photonics at scale[15], and promising centres in hosts such as SiC are being developed[16,17] in tandem with the development of SiC integrated photonics[18]. By contrast, the silicon-integrated photonics platform boasts decades of maturity, including best-in-class integrated single-photon detectors[19], a vast library of quantum optics components[20] and the ability to directly leverage the global semiconductor microelectronics industry.

The appeal of photon–spin centres in silicon photonic networks has spurred the development of hybrid platforms combining non-silicon photon–spin host materials with silicon photonics[21]. However, some of the longest spin coherence times ever measured have been in the silicon host itself[3,22], which can be isotopically purified to remove the magnetic noise due to the spin $\frac{1}{2}$ ^{29}Si nuclear spins. Identifying suitable individually addressable photon–spin centres in silicon could obviate the need to duplicate the development of integrated photonics in an entirely new, and more challenging, material platform.

Despite this opportunity, single spins had not been detected optically in silicon. Single spins without optical access have been detected electrically in silicon[23–30], single spins have been driven optically and detected electrically[31], and single centres without electron spins have been recently observed[32]. Yet the key goal of imaging individual spins has remained elusive for silicon. Unfortunately, the most widely studied silicon photon–spin centres, phosphorus[33], selenium[34] and erbium[31,35], do not emit brightly. Recently, the T centre[36,37] was identified as a photon–spin interface in silicon combining long-lived electron (>2 ms) and nuclear (>1.1 s) spins and sharp, spin-dependent telecommunications-band optical transitions. This combination is exceedingly rare among photon–spin centres across all solid-state hosts studied so far[38].

In this work we produce tens of thousands of individually addressable 'micropucks' in commercial silicon-on-insulator (SOI) integrated photonic wafers and, using cryogenic confocal microscopy, confirm that each of the micropucks measured has a small number of individually addressable T centres. We resolve the spin-dependent transitions of individual spins for a subset of these T centres subject to a small magnetic field. We initialize and measure single spin states and perform an all-optical spin lifetime measurement. This represents the optical identification of single spins in silicon, and directly paves the way for the development of telecommunications-band, silicon-integrated global quantum technology networks.

The T centre

The T centre[36,39] is a radiation damage centre in silicon comprising two carbon atoms, one hydrogen atom and an unpaired electron (Fig. 1a).

[1]Department of Physics, Simon Fraser University, Burnaby, British Columbia, Canada. [2]Photonic Inc., Coquitlam, British Columbia, Canada. [3]Department of Physics, University of Montréal, Montréal, Quebec, Canada. [4]These authors contributed equally: D. B. Higginbottom, A. T. K. Kurkjian. ✉e-mail: s.simmons@sfu.ca

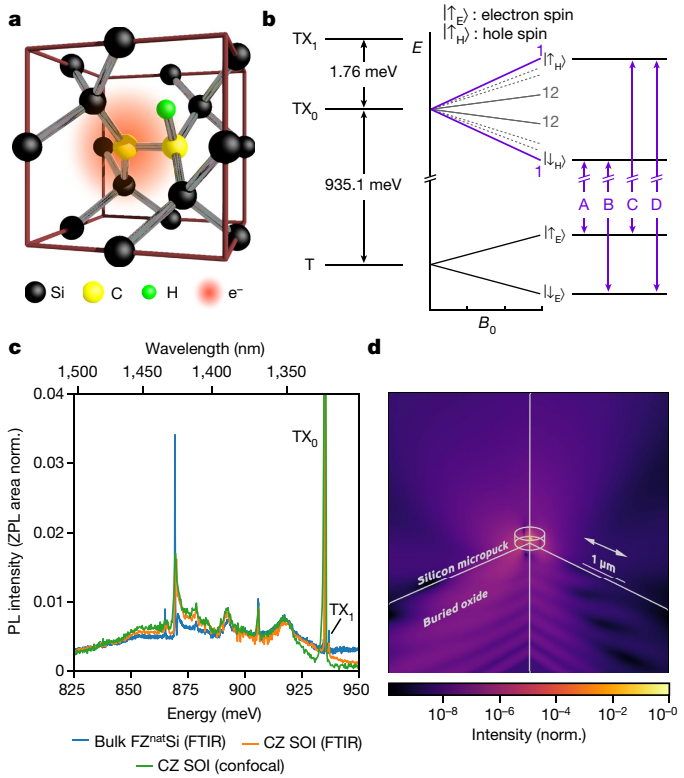

Fig. 1 | Integrating and optically coupling the T centre. a, T centre chemical structure and **b**, electronic level structure[36]. The two lowest energy bound exciton states are TX_0 and TX_1. In a magnetic field the optical transition between TX_0 and the ground state splits into four spin-dependent optical transitions, A, B, C and D, depending on centre orientation. **c**, PL spectra of T centres in bulk natural float zone (FZ) silicon (blue), natural Czochralski (CZ) SOI wafer (orange) and patterned SOI measured confocally (green, instrument resolution limited). Spectra are normalized (norm.) to ZPL area. FTIR, Fourier transform infrared. **d**, Simulated emission profile of a T centre at the centre of a 305 nm radius micropuck, where the arrow indicates dipole orientation. Normalized emission intensity (colour axis) is shown on two perpendicular cross-sectional planes.

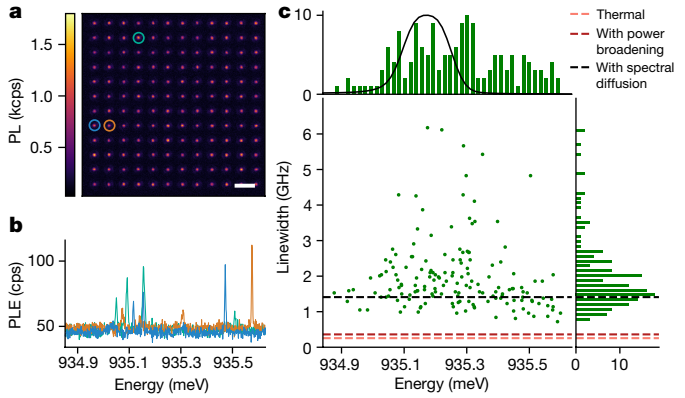

Fig. 2 | Single centres in silicon. a, PL raster of 305-nm radius micropucks. Scale bar, 10 µm. **b**, Characteristic PLE spectra of individual micropucks circled in **a** showing discrete T centre resonances. Fluorescence is collected on the T centre PSB. **c**, Scatterplot and histograms of T ZPL energies (top) and linewidths (right) from all 144 micropucks shown in **a**. The prepatterning PL spectrum from Fig. 1c is included for comparison (top, black line).

With a zero-phonon line (ZPL) optical transition at 935.1 meV (1,326 nm), the T centre is one of a class of silicon radiation damage centres that are known to emit light in the near-infrared telecommunication bands[40]. Measurements of T centre ensembles in isotopically enriched ^{28}Si found an excited-state lifetime of 940 ns, and ensemble transition linewidths as low as 33 MHz (ref. [36]).

The T centre ground state features an unpaired electron spin and a hyperfine-coupled hydrogen nuclear spin. Both the ground state electron and hydrogen nuclear spins are long-lived, with coherence times greater than 2.1 ms and 1.1 s, respectively, in ^{28}Si (ref. [36]). Within the bound exciton optically excited state, the two electrons form a singlet and the reduced symmetry of the defect splits the hole states into two spin doublets, labelled TX_0 and TX_1 (Fig. 1b). Under a static magnetic field, the TX_0 ZPL splits into four spin-dependent transitions. Each T centre belongs to one of 12 orientational subsets, each with their own effective hole spin Landé factor g_H that determines the level splittings. The anisotropic hole g tensor produces effective g_H values between 0.85 and 3.50 depending on the magnetic field[36,39].

Photonic integration

We begin by generating T centres in industry-standard SOI chips[37]. As shown in Fig. 1c, T centre photoluminescence (PL) dominates the sample's spectrum. To spatially resolve individual T centres, experiments are conducted within a home-built cryogenic confocal microscope measuring 4.3(3) K at the SOI device layer (Methods).

The TX_0 ZPL homogeneous linewidth has a temperature-dependent lower bound, given by the thermal activation between TX_0 and TX_1 (ref. [36]). This broadening is negligible at 1.5 K, but at 4.3 K bounds the linewidths of individual emitters above 255 MHz. Furthermore, we expect spectral diffusion on the order of 1 GHz in this material[37] and power broadening from resonant optical driving. The large inhomogeneous broadening observed, more than 37 GHz, indicates that individual T centres with 1 GHz linewidth would be spectrally addressable if sufficiently low concentrations can be isolated spatially. In this work, we resonantly excite single T centres with a tuneable single-frequency laser and collect photons emitted into the phonon sideband (PSB), a technique known as PL excitation (PLE) with spectral resolution $\ll$1 GHz (Methods).

SOI is a leading photonics platform in part because the high refractive index of silicon ($n \cong 3.5$ at 1,326 nm) efficiently traps light within the device layer by total internal reflection. This poses a challenge for microscopy on unpatterned SOI, in which extraction efficiencies are on the order of 0.5%. Yet luminescence from individual G centres isolated in Si by confocal microscopy[32] can be up to 16 kilocounts per second (kcps)[41]. For longer-lived centres such as T, it is advantageous to enhance luminescence through photonic design. Luminescence from a solid-state emitter may be improved using nanophotonic structures, such as planar bullseye gratings[42] and vertical pillar cavities[43]. We take a similar approach by fabricating 150,000 'micropucks' on chip. Compared to unpatterned SOI, micropucks increase the out-coupling of light from an emitter by Purcell enhancing emission and by shaping the profile to improve collection efficiency. Figure 1d shows the simulated field of a dipole emitter at the micropuck centre, oriented in the device plane. We estimate up to a 58-fold ZPL intensity improvement over a centre in unpatterned SOI.

Resonant excitation of single centres

Confocal PLE reveals evidence of addressable single T centres. We select a set of 305 nm radius micropucks (Fig. 2a) and then, for each micropuck, measure PLE spectra over a 776 µeV range around the bulk TX_0 ZPL. Three example single-puck PLE spectra are shown in Fig. 2b. Each PLE spectrum contains a small number (on average 1.1) of narrow resonances sampled from the larger inhomogeneous distribution. The sparse and resolvable T centres in each micropuck, some with linewidths 40 times narrower than the inhomogeneous linewidth,

provide strong evidence that this sample offers tens of thousands of individually addressable T centres for study. From the occurrence of discrete T PLE resonances we infer a lower bound centre concentration of 1.7×10^{13} cm^{-3}.

We detect up to 325 cps of sideband fluorescence from our brightest micropuck-coupled T centres, or 2.1 kcps after accounting for measured detection losses (Extended Data Table 2). This compares favourably to fluorescence rates from prominent telecom photon–spin centres in Si. Er^{3+}, for example, fluoresces at only 500 cps assuming perfect coupling and no losses at all[35]. From the bulk T centre lifetime of 940 ns, the sideband relative intensity at r = 305 nm, the spectral collection range of $\lambda > 1.35$ μm and the same measured detection losses (Extended Data Table 2), we expect 11.6 kcps from an optimally coupled, saturated, unit radiative efficiency T centre. This leaves a factor of 36 accounted for by some combination of incomplete saturation, uncharacterized losses (for example, single-mode coupling), suboptimal coupling to the micropuck (for example, T centre position and orientation) and potentially non-radiative decay.

Figure 2c shows the T centre ZPL peak positions and linewidths found within the 144 micropucks in Fig. 2a. The ZPL peak distribution results from variations in isotopic and strain environments local to each defect. This inhomogeneous distribution is broader and slightly shifted from the unpatterned SOI ZPL (Fig. 1c), shown overlaid. A histogram of individual linewidths drawn from this scatterplot is shown in Fig. 2c (right) and matches our expectations for single centres in SOI at this temperature. At saturation power, roughly the power chosen for this study, a typical line will be power broadened from the thermal lower bound (255 MHz) to 361 MHz absent spectral diffusion. Including the characteristic spectral diffusion of this material (1 GHz), the typical power-broadened linewidth we expect is 1.41 GHz, which largely accounts for the median of our measured distribution linewidth of 1.68 GHz.

In nearby 846-nm radius micropucks, we measure low-power T centre ZPL lines as narrow as 660 MHz, from which we conclude that a selection of centres experience less than 400 MHz total spectral diffusion in this heavily damaged and unoptimized material. As noted in ref. [37], surface optimization[44], electrostatic control[45] and lower levels of implantation damage[46,47] have all been shown to notably reduce environmental noise and spectral diffusion for other colour centres, and similar techniques may be applied to this system.

Single spins in silicon

We observe and characterize the signature spin-selective optical transitions of several individually addressable T centre spins in a static magnetic field. The magnetic field B_0 splits the ground state isotropic electron spin states $|\uparrow_E\rangle, |\downarrow_E\rangle$ as well as the excited-state bound exciton anisotropic hole spin states $|\uparrow_H\rangle, |\downarrow_H\rangle$. Under these conditions the four spin-selective transitions A, B, C and D shown in Fig. 1b are detuned from the zero-field ZPL by Δ according to:

$$\Delta_{A,B,C,D} = \frac{1}{2}\mu_B \left| B_0 \right| (\mp g_{E,i} \mp g_{H,i}), \quad (1)$$

where the μ_B is the Bohr magneton and $g_{E,i}$, $g_{H,i}$ are the electron and hole Landé g factors for orientation i in the specific magnetic field B_0. Owing to g_H anisotropy, the 12 orientational T centre subsets split differently for low-symmetry magnetic field directions.

We mount the sample on a permanent SmCo magnet such that the magnetic fringe field magnitude and orientation varies with position. From simulations we estimate 40 mT < $|B_0|$ < 160 mT over the device layer of the chip. Given zero-field ZPL linewidths as low as 660 MHz this field is sufficient to split and resolve all four spin-selective optical transitions A, B, C and D for some T centre orientations.

As in previous bulk experiments[36], performing single-frequency PLE spectroscopy in a magnetic field results in almost no signal due to electron spin hyperpolarization as the laser scans over the A, B, C and D transitions sequentially. The PLE signal that remains is from the subsets of spins whose B and C transitions overlap, in which no spin shelving state is available and hyperpolarization does not occur. In ref. [36]. PLE signal from the hyperpolarized (dark) subsets was recovered by depolarizing the spins using magnetic resonance. In this work we depolarize the electron spins by performing two-colour PLE. Specifically, we scan two single-frequency lasers over an individual T centre's ZPL transition energy and observe fluorescence whenever the lasers simultaneously address optical transitions corresponding to the two electron spin states.

In Fig. 3a–c we show two-colour PLE spectra of three T centres taken from separate 305-nm radius micropucks. Each TX_0 ZPL splits differently, reflecting varying orientations. T centre 1 has nearly degenerate B and C transitions, and each laser independently drives continuous fluorescence. By contrast, the B and C transitions of T centre 2 are well resolved with 1 GHz splitting. The brightest fluorescence is produced at two-colour combinations in which the lasers are detuned from each other and separately resonant with transitions B and C. Extra peaks reveal transitions A and D (shown in Fig. 3b). The B–C splitting of T centre 3 is only 0.7 GHz, but the two A–D resonances remain well resolved.

We perform pump-probe PLE measurements of T centre 2 by fixing one 'pump' laser at a spin-selective transition and scanning the frequency of the second 'probe' laser. The coloured lines in Fig. 3d are probe spectra for a pump at each of the transitions A, B, C and D as indicated by a text label and same-colour arrow. For each pump frequency two resonances are visible, corresponding to the two optical transitions of the electron spin state unaddressed by the pump. A single-frequency PLE scan for reference, in black, shows the weak single-laser resonance at the overlap of the B and C transitions.

Fitting equation (1) to the peak positions and order gives $|B_0|$ = 88.1(7) mT (consistent with the simulated magnetic field at these chip coordinates), and g_H = 2.76(2). We assume the bulk value of g_E = 2.005(8) (ref. [36]). We further fit a four-level optical Bloch Hamiltonian to the pump-probe spectra with a thermal linewidth of 255 MHz corresponding to 4.3 K, 800(40) MHz Gaussian spectral diffusion and optical Rabi frequencies 10(1) and 14(1) MHz for lasers 1 and 2, respectively. Pump-probe measurements with an adjustable magnetic field demonstrate that the TX_0 splitting is magnetic field tuneable (Supplementary Information) and confirm the electronic configuration (Fig. 1b).

Photon autocorrelation measurements made with a Hanbury Brown–Twiss detector confirm these spins are single. Sideband fluorescence is recorded under two-colour excitation of the B and C transitions. Figure 3e shows the resulting background-subtracted correlation function, $g^2(\tau)$, and the same fitted four-level optical Bloch model. The zero-delay coincidence rate is $g^2(0) = 0.20(6)$, significantly below the single-photon witness level $g^2(0) < 0.5$.

Having confirmed these are single spins, we next initialize and read the spin states optically and perform a spin lifetime (T_1) measurement. The B and C transitions of T centre 3 are addressed with the optical pulse sequence shown in Fig. 3f. B (C) pulses prepare up (down) polarized spin states by optical pumping. For $t_{wait} \ll T_1$, pulses 1 and 3 pump the spin to an opposing spin state through TX_0 and produce an accompanying luminescence transient equal to the area difference between consecutive B (C) pulses as inset in Fig. 3f. As t_{wait} approaches and exceeds T_1 the prepared spin has time to relax to a mixed equilibrium state between pulses and the spin transient vanishes. Residual optical fields due to optical pulse extinction slowly pump the spin to a mixed state during t_{wait} and artificially shorten T_1 below the bulk electron spin lifetime $T_{1E} \gg 1$ s (ref. [36]). This effect is visible as the wait time approaches 1 ms and causes asymmetric transient lifetimes of 0.85(6) and 1.2(1) ms for the B (orange) and C (blue) read pulses respectively. More optical extinction will extend the measurable spin lifetime in future work.

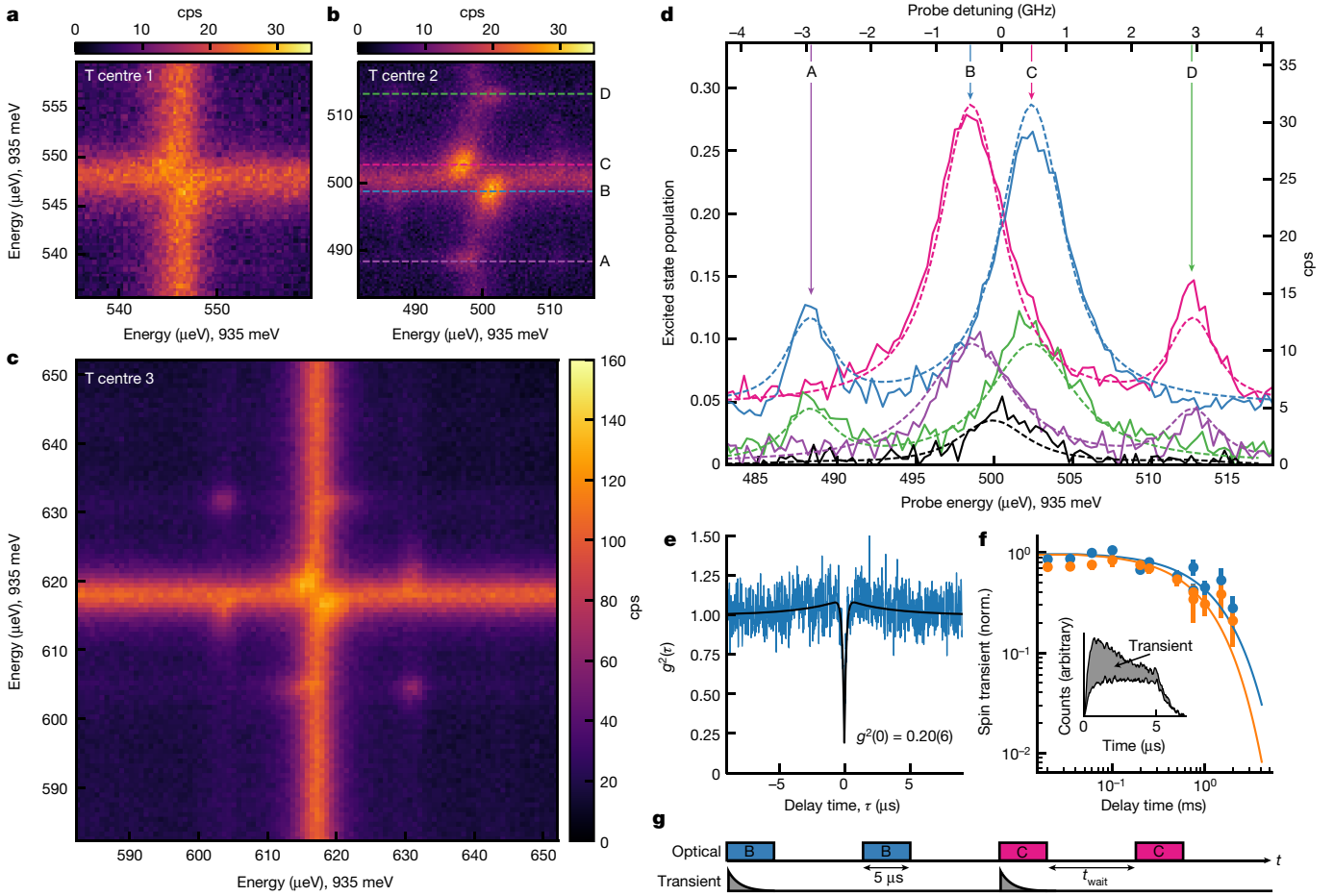

Fig. 3 | Single-spin optical initialization and readout. a–**c**, Two-colour PLE of three T centres showing varying degrees of splitting. **d**, Scanning a single probe laser over T centre 2 produces only weak fluorescence at the overlap of transitions B and C (black). When pumping spin-selective transitions (labelled, arrows), the corresponding probe spectra (coloured) feature two transitions from the unpumped spin state. Dashed lines are a fitted four-level model. **e**, Background-corrected autocorrelation measurement of two-colour PLE fluorescence (blue) confirms each spin is single. The four-level model (black) reproduces the correlation function. **f**, Fluorescence transient decaying as a function of t_{wait}. The inset to **f** illustrates how, for each of those delay times, the transient area is determined from the difference between two fluorescence curves. **g**, Pulsed excitation sequence used.

Conclusion and outlook

We have optically detected individual spins in silicon. We create tens of thousands of silicon photonic devices, each integrating a small handful of spectrally resolvable and optically accessible T centre spin qubits, leveraging industry-standard photonic SOI wafers and processing. These devices show single-centre T transitions 40 times narrower than the inhomogeneously broadened transition, with $g^2(0) = 0.20(6) < 0.5$. When placed in a magnetic field, T centre spin qubits offer spin-selective optical transitions in the telecommunications O band, and we characterize these transitions for a subset of individual centres using two-colour resonant excitation spectroscopy at temperatures above 4.2 K. We optically initialize and measure a single electron spin in silicon and measure the spin lifetime with an optical pulse sequence.

We measured device-integrated T centres that will have sub-400 MHz long-term optical linewidths below 2.5 K. The long-term optical linewidths of many emitters have been improved by fabrication process development, electrostatic engineering and dynamic control. However, even the present linewidths are useful for quantum devices using established silicon photonics. Silicon photonic cavities can be made reproducibly with mode volumes of $(\lambda/n)^3$ and Q factors exceeding a million on this very platform[48], but only cavity Qs of $1–2 \times 10^5$ are required to Purcell enhance these centres such that their ZPL emission rate surpasses 1 GHz. These cavity-enhanced T devices would produce spin-entangled O-band photons with near-unit efficiency and 60% indistinguishability on chip without filtering, and could make immediate use of integrated silicon photonic networks boasting low-loss passive and active components, high-efficiency (95%) coupling to industry-standard telecom fibres and on-chip single-photon detectors with efficiencies of 99%. Taken together, this work demonstrates that silicon T centres are a suitable technological backbone for commercial-scale, telecommunications-linked, near-term quantum computing and communication networks.

Online content

Any methods, additional references, Nature Research reporting summaries, source data, extended data, supplementary information, acknowledgements, peer review information; details of author contributions and competing interests; and statements of data and code availability are available at https://doi.org/10.1038/s41586-022-04821-y.

1. Kimble, H. J. The quantum internet. *Nature* **453**, 1023–1030 (2008).
2. Pompili, M. et al. Realization of a multinode quantum network of remote solid-state qubits. *Science* **372**, 259–264 (2021).
3. Saeedi, K. et al. Room-temperature quantum bit storage exceeding 39 minutes using ionized donors in silicon-28. *Science* **342**, 830–833 (2013).
4. Bernien, H. et al. Heralded entanglement between solid-state qubits separated by three metres. *Nature* **497**, 86–90 (2013).

5. Delteil, A., Sun, Z., Fält, S. & Imamoğlu, A. Realization of a cascaded quantum system: heralded absorption of a single photon qubit by a single-electron charged quantum dot. *Phys. Rev. Lett.* **118**, 177401 (2017).
6. Pfaff, W. et al. Unconditional quantum teleportation between distant solid-state quantum bits. *Science* **345**, 532–535 (2014).
7. Hensen, B. et al. Loophole-free Bell inequality violation using electron spins separated by 1.3 kilometres. *Nature* **526**, 682–686 (2015).
8. Bhaskar, M. K. et al. Experimental demonstration of memory-enhanced quantum communication. *Nature* **580**, 60–64 (2020).
9. Raha, M. et al. Optical quantum nondemolition measurement of a single rare earth ion qubit. *Nat. Commun.* **11**, 1605 (2020).
10. Tian, Z. et al. Optically addressing single rare-earth ions in a nanophotonic cavity. *Phys. Rev. Lett.* **121**, 183603 (2018).
11. Gottscholl, A. et al. Initialization and read-out of intrinsic spin defects in a van der Waals crystal at room temperature. *Nat. Mater.* **19**, 540–545 (2020).
12. Hayee, F. et al. Revealing multiple classes of stable quantum emitters in hexagonal boron nitride with correlated optical and electron microscopy. *Nat. Mater.* **19**, 534–539 (2020).
13. Gruber, A. et al. Scanning confocal optical microscopy and magnetic resonance on single defect centers. *Science* **276**, 2012–2014 (1997).
14. Doherty, M. W. et al. The nitrogen-vacancy colour centre in diamond. *Phys. Rep.* **528**, 1–45 (2013).
15. Wan, N. H. et al. Large-scale integration of artificial atoms in hybrid photonic circuits. *Nature* **583**, 226–231 (2020).
16. Wolfowicz, G. et al. Vanadium spin qubits as telecom quantum emitters in silicon carbide. *Sci. Adv.* **6**, eaaz1192 (2020).
17. Falk, A. L. et al. Polytype control of spin qubits in silicon carbide. *Nat. Commun.* **4**, 1819 (2013).
18. Lukin, M. D. et al. 4H-silicon-carbide-on-insulator for integrated quantum and nonlinear photonics. *Nat. Photonics* **14**, 330–334 (2020).
19. Akhlaghi, M. K., Schelew, E. & Young, J. F. Waveguide integrated superconducting single-photon detectors implemented as near-perfect absorbers of coherent radiation. *Nat. Commun.* **6**, 8233 (2015).
20. Thomson, D. et al. Roadmap on silicon photonics. *J. Opt.* **18**, 073003 (2016).
21. Dibos, A. M., Raha, M., Phenicie, C. M. & Thompson, J. D. Atomic source of single photons in the telecom band. *Phys. Rev. Lett.* **120**, 243601 (2018).
22. Tyryshkin, A. M. et al. Electron spin coherence exceeding seconds in high-purity silicon. *Nat. Mater.* **11**, 143–147 (2012).
23. Morello, A. et al. Single-shot readout of an electron spin in silicon. *Nature* **467**, 687–691 (2010).
24. Pla, J. J. et al. A single-atom electron spin qubit in silicon. *Nature* **489**, 541–545 (2012).
25. Maune, B. M. et al. Coherent singlet-triplet oscillations in a silicon-based double quantum dot. *Nature* **481**, 344–347 (2012).
26. Büch, H., Mahapatra, S., Rahman, R., Morello, A. & Simmons, M. Y. Spin readout and addressability of phosphorus-donor clusters in silicon. *Nat. Commun.* **4**, 2017 (2013).
27. Veldhorst, M. et al. An addressable quantum dot qubit with fault-tolerant control-fidelity. *Nat. Nanotechnol.* **9**, 981–985 (2014).
28. Kawakami, E. et al. Electrical control of a long-lived spin qubit in a Si/SiGe quantum dot. *Nat. Nanotechnol.* **9**, 666–670 (2014).
29. Mi, X. et al. A coherent spin-photon interface in silicon. *Nature* **555**, 599–603 (2018).
30. Crippa, A. et al. Gate-reflectometry dispersive readout and coherent control of a spin qubit in silicon. *Nat. Commun.* **10**, 2776 (2019).
31. Yin, C. et al. Optical addressing of an individual erbium ion in silicon. *Nature* **497**, 91–94 (2013).
32. Redjem, W. et al. Single artificial atoms in silicon emitting at telecom wavelengths. *Nat. Electron.* **3**, 738–743 (2020).
33. Kane, B. E. A silicon-based nuclear spin quantum computer. *Nature* **393**, 133–137 (1998).
34. DeAbreu, A. et al. Characterization of the Si: Se+ spin-photon interface. *Phys. Rev. Appl.* **11**, 44036 (2019).
35. Kenyon, A. J. Erbium in silicon. *Semiconduct. Sci. Technol.* **20**, R65–R84 (2005).
36. Bergeron, L. et al. Silicon-Integrated telecommunications photon-spin interface. *PRX Quantum* **1**, 20301 (2020).
37. MacQuarrie, E. R. et al. Generating T centres in photonic silicon-on-insulator material by ion implantation. *New J. Phys.* **23**, 103008 (2021).
38. Zhang, G., Yuan, C., Chou, J. P. & Gali, A. Material platforms for defect qubits and single-photon emitters. *Appl. Phys. Rev.* **7**, 31308 (2020).
39. Safonov, A. N., Lightowlers, E. C. & Davies, G. Carbon-hydrogen deep level luminescence centre in silicon responsible for the T-line. *Mater. Sci. Forum* **196-201**, 909–914 (1995).
40. Chartrand, C. et al. Highly enriched Si 28 reveals remarkable optical linewidths and fine structure for well-known damage centers. *Phys. Rev. B.* **98**, 195201 (2018).
41. Durand, A. et al. Broad diversity of near-infrared single-photon emitters in silicon. *Phys. Rev. Lett.* **126**, 083602 (2021).
42. Li, L. et al. Efficient photon collection from a nitrogen vacancy center in a circular bullseye grating. *Nano Lett.* **15**, 1493–1497 (2015).
43. Ding, X. et al. On-demand single photons with high extraction efficiency and near-unity indistinguishability from a resonantly driven quantum dot in a micropillar. *Phys. Rev. Lett.* **116**, 020401 (2016).
44. Sangtawesin S. et al. Origins of diamond surface noise probed by correlating single-spin measurements with surface spectroscopy. *Phys. Rev. X.* **9**, 031052 (2019).
45. Anderson, C. P. et al. Electrical and optical control of single spins integrated in scalable semiconductor devices. *Science* **366**, 1255–1230 (2019).
46. Van Dam, S. B. et al. Optical coherence of diamond nitrogen-vacancy centers formed by ion implantation and annealing. *Phys. Rev. B.* **99**, 161203 (2019).
47. Wolfowicz, G. et al. Awschalom. Quantum guidelines for solid-state spin defects. *Nat. Rev. Mater.* **6**, 906–925 (2021).
48. Ashida, K. et al. Ultrahigh-Q photonic crystal nanocavities fabricated by CMOS process technologies. *Opt. Express* **25**, 18165 (2017).

Methods

Implant and anneal recipe

Our sample is commercial SOI with a 220-nm thick, P-type Czochralski ^{nat}Si device layer and 3-μm thick buried oxide layer. High concentrations of T are created in the device layer by separately implanting carbon-13 and hydrogen, annealing after each implant. Implants were performed by Cutting Edge Ions. Implant energies for the carbon (38 keV) and hydrogen (9 keV) produce overlapping implant profiles at the device layer centre (110 nm depth). Equal doses of 7×10^{12} cm^{-2} are chosen from an implant optimization study reported in ref. [37]. Postimplant secondary ion mass spectroscopy measurements confirm carbon is introduced at above the carbon solubility limit. After the initial carbon implant, we rapidly thermally annealed the sample at 1,000 °C for 20 s in argon to repair lattice damage and substitute the implanted carbon. After the hydrogen implant, the sample is boiled for 1 h in deionized water and, finally, rapidly thermally annealed at 420 °C for 3 min.

Fourier transform infrared spectroscopy

The PL spectra of prepatterned SOI and bulk ^{nat}Si samples are measured using a Fourier transform infrared spectrometer. The samples are mounted in a liquid He immersion cryostat and excited above-bandgap using a 532 nm diode laser with a spot size of 3 mm. Fluorescence is analysed by a Bruker IFS 125HR spectrometer to a spectral resolution of 62 μeV.

Photonics patterning

The implanted SOI chip was subsequently patterned by e-beam lithography at Applied Nanotools integrated photonics foundry using a negative-tone hydrogen silsesquioxane process. The chip design includes 150,000 micropucks with radii between 0.25 and 1.1 μm, as well as larger unpatterned silicon blocks up to several 100 μm wide.

Confocal microscopy

The sample is mounted in a low-noise, high optical access cryostat (Montana Instruments s100) with a base temperature of 2.7 K. Closed-loop piezoelectric positioners (Attocube, two ANPx101 and one ANPz102) inside the cryostat position the sample along three axes of motion with a 5 mm range and roughly 1–2 μm precision. A numerical aperture (NA) 0.71 microscope objective (SEIWA PE IR 2000HR) is mounted above a fused silica cryostat window. Further precise lateral movement is provided by two room temperature piezo positioners (Physik Instrumente P517) that shift the objective by up to 100 μm with 10 nm precision. The confocal microscope images the sample to a single-mode fibre with a calculated resolution of 1 μm.

In the confocal setup, PL is generated with a 978-nm diode laser (QPhotonics QFBGLD-980-5). This above-bandgap light creates free carriers in the silicon that travel and subsequently bind to centres and fluoresce on recombination. Fluorescence collected by the microscope is directed to either a spectrometer or detector. PL spectra are measured with a fibre-coupled diffraction grating spectrometer (Princeton SpectraPro HRS-300) imaged onto an ultra-low-noise LN cooled InGaAs camera (Princeton NIRvana-LN), with a 150 groove per mm grating that provides 1 nm spectral resolution. When using the confocal microscope for imaging or recording PLE spectra, fluorescence is directed to either a fibre-coupled avalanche photodiode (IDQuantique ID230) configured for 15% quantum efficiency or a fibre-coupled superconducting nanorwire single-photon detector (SNSPD) (IDQuantique ID281) with 70% efficiency. Photon arrival times are recorded with an IDQuantique ID900 time controller. PL images are taken with a $\lambda > 1.35$ μm (932 meV) longpass filter that isolates the T centre PSB.

We measure confocal PLE spectra using a continuously tuneable diode laser (Toptica CTL 1320) locked to a wavemeter (Bristol 871) with 0.01 pm precision and 1 pm accuracy. Typical laser power at the Si surface is roughly 9 μW, the power inside the Si material is 7 μW accounting for polarization-averaged Fresnel reflection at the surface. The collected PL sideband intensity is measured with the avalanche photodiode or SNSPD. Two-colour PLE is performed with two CTL/Bristol pairs or two Nanoplus diode lasers calibrated to a Bristol wavemeter. We filter the sideband fluorescence for $\lambda > 1.35$ μm (918 meV) in single-colour PLE and $\lambda > 1.40$ μm (886 meV) in two-colour PLE experiments.

Sample thermometry

The temperature of the sample is estimated in situ from confocal PL spectra of the T centre. PL from a 200×200 μm^2 SOI block section (included on the chip design as a 'bulk' SOI reference) is directed into the single-photon spectrometer. The integrated luminescence ratio of the ZPLs arising from the thermally populated TX_0 and TX_1 levels, as shown in Fig. 1c, reveals a temperature of 4.3(3) K (ref. [49]).

Micropucks

The radius of a micropuck determines the wavelength-dependent 'relative intensity' of any emitters contained within it. Here the relative intensity ($I_r(\lambda)$) of the emitter compared to a homogeneous silicon environment is given by the product of its collection efficiency ($\eta_{obj}(\lambda)$) and its Purcell factor ($P_F(\lambda)$). Extended Data Fig. 1b shows the relative intensity collected into an NA 0.7 objective as a function of micropuck radius r according to simulations. Similar simulations reveal a modest single-wavelength Purcell enhancement with a range of 0.8 to 3.5, roughly periodic with $2nr/\lambda$. With this information we determine the optimal micropuck radii for PL and PLE measurements of individual optimally positioned T centres. For example, the maximum 58-fold ZPL intensity improvement between a centred planar T centre in a micropuck compared to a similarly positioned T centre in unpatterned SOI is attained at 520 nm radius.

The solid blue line in Extended Data Fig. 1c is the collected ZPL intensity according to simulations. It is I_r integrated over the bulk T centre ZPL or, equivalently, the product of $I_r(\lambda = 1{,}326$ nm) and the T centre Debye–Waller factor 0.23 (ref. [36]). The solid red line in Extended Data Fig. 1c is the collected T centre PSB intensity, which we arrive at by integrating $I_r(\lambda)$ over the bulk T centre PSB spectrum[36], specifically 1,330 to 1,600 nm.

We confirm these predictions experimentally. Extended Data Fig. 1a shows a rastered confocal microscope PL image of a block of micropucks with radii that increment from 250 nm (upper left) to 850 nm (lower right). The micropucks are excited with 978 nm above-bandgap light and the detected fluorescence is filtered to detect wavelengths longer than 1,330 nm. As expected, there is a clear periodic variation in integrated intensity with radius, as well as a steady increase in intensity with radius corresponding to the increasing number of T centres in larger micropucks. We find reasonable agreement between the PSB micropuck intensity (red points, Extended Data Fig. 1c) and the simulated PL intensity (red curve, Extended Data Fig. 1c), even though many fluorescent centres, including G centres and several T centres, contribute to the measured signal at these wavelengths using PL.

We also find good agreement with the collected T centre ZPL intensity in PL as a function of micropuck radius (blue points and blue line, Extended Data Fig. 1c). The blue points in Extended Data Fig. 1c are the area of a Gaussian–Lorentzian product fit to each ZPL.

Finite difference time domain (FDTD) simulations

Three-dimensional FDTD simulations were performed using Lumerical FDTD to compare the collection efficiency $\eta_{obj}(\lambda)$ and Purcell factor $P_F(\lambda)$ from a planar dipole emitter in both an un-etched SOI device layer and silicon micropuck into an NA 0.7 microscope objective. The relative intensity $I_r(\lambda)$ collected into the objective compared to the total centre fluorescence in a homogeneous medium is

$$I_r(\lambda) = \eta_{obj}(\lambda) P_F(\lambda) \quad (2)$$

For each of these parameters (I_r, η_{obj} and P_F) we can derive spectrally weighted integrals corresponding to the intensity, Purcell or efficiency over a useful wavelength range. The weighting function for this integral is the area-normalized bulk T centre spectrum I_T (ref. [36]). For example, we may calculate the relative intensity of the T centre PSB:

$$I_r^{PSB} = \int_{1,330\ nm}^{1,600\ nm} I_r(\lambda) I_T(\lambda) d\lambda. \quad (3)$$

A comparison between the simulated collection efficiency, Purcell factor and relative intensity in un-etched SOI and the micropucks is provided in Extended Data Fig. 2.

The weighted I_r for a 305-nm micropuck is provided in Extended Data Table 1 for the five spectral regions corresponding to the T ZPL, the PL detection range, the PLE detection range, the two-colour PLE detection range and the total T centre spectrum.

Micropuck PL spectra

We measure the PL spectra of micropucks using an ultra-low light spectrometer as described in the Methods. In Extended Data Fig. 3 we show spectra for an example selection of individual micropucks of various sizes. The TX_0 ZPL evident at 935 meV confirms the presence of T in most of these structures. In addition to T, we also see the G centre ZPL at 969 meV. The T, G ZPL peak amplitudes depend sensitively on micropuck radius as the relative intensity enhancement band shifts with radius according to Extended Data Fig. 1b. It can also be seen that particular micropuck radii enhance emission on the T PSB, which is advantageous for PLE measurements. T ZPL areas and integrated PSBs for the complete dataset are shown as a function of radius in Extended Data Fig. 1c.

PLE count rate analysis

The expected maximum (saturated) count rate from a single T centre is the product of the homogeneous decay rate (halved for saturated resonant excitation), the Purcell factor and various emission and collection efficiencies, some of which remain unknown. The most significant of these unknowns is the radiative efficiency of the T centre, that is the proportion of decay events that are radiative, which is expected to be near unity[36]. The measured efficiencies relevant to our 305-nm micropuck PLE measurements are listed in Extended Data Table 2. The micropuck effect captures both the Purcell and the collection efficiency and is given by the relative intensity I_r, with values presented previously in Extended Data Table 1.

PLE linewidth analysis

Our starting point for zero-field PLE linewidth analysis are the Bloch equations for a two-level atom in a classical field[50]. The steady-state excited-state population is

$$\rho_{ee} = \frac{1}{2} \frac{\Omega^2}{\left(\frac{\Gamma\Delta^2}{\gamma_t} + \gamma_t\Gamma + \Omega^2\right)}, \quad (4)$$

where $\Omega = d \cdot E$ is the excitation Rabi frequency, Δ is the detuning of the field from the transition, Γ is the excited-state decay rate and $\gamma_t = \gamma + \Gamma/2$ where γ is the transition dephasing rate. At the temperatures studied here, $\gamma \gg \Gamma$ and $\gamma_t \cong \gamma$. Also $\rho_{ee} < \frac{1}{2}$ and approaches $\frac{1}{2}$ in the high power limit; ρ_{ee} is Lorentzian in the field detuning Δ with full-width at half-maximum (FWHM)

$$w = 2\sqrt{\gamma_t^2 + \Omega^2 \frac{\gamma_t}{\Gamma}}, \quad (5)$$

where the leftmost part of the sum is the low-power linewidth and the rightmost part of the sum is the linewidth contribution from power broadening.

We define saturation power as Ω_s such that $\rho_{ee}(\Omega = \Omega_s, \Delta = 0) = \frac{1}{2}\max(\rho_{ee}) = \frac{1}{4}$, giving $\Omega_s = \sqrt{\gamma_t\Gamma}$. The saturation Rabi frequency we expect for T at 4.3 K in the absence of spectral diffusion is $\Omega_s = 4.64 \times 2\pi$ MHz.

The linewidth at saturation power is therefore

$$w_s = 2\sqrt{2}\gamma_t, \quad (6)$$

or $\sqrt{2}$ larger than the zero-power linewidth. From this relationship we arrive at an estimated saturation power linewidth of 361 MHz from a thermal dephasing of $\gamma_t = 127.5 \times 2\pi$ MHz or a thermal linewidth of 255 MHz.

To include spectral diffusion, we can follow the same process, but we must first convolve equation (4) by an area-normalized Gaussian spectral diffusion function $G(\Delta)$ with half-width at half-maximum (HWHM) $\gamma_{s.d.}$ (defined as a HWHM for notational consistency with γ_t):

$$\rho'_{ee} = \rho_{ee} * G = \int_{-\infty}^{\infty} \rho_{ee}(\Delta) G(\Delta' - \Delta) d\Delta. \quad (7)$$

We perform this convolution numerically to find the saturation power Ω'_s such that $\rho'_{ee}(\Omega, \Delta' = 0) = \frac{1}{4}$ and then the FWHM of the spectrally diffused line at $\Omega = \Omega'_s$ by numerically solving $\rho'_{ee}(\Omega = \Omega'_s, \Delta') = \frac{1}{8}$. By this method we arrive at a power-broadened linewidth of 1.41 GHz for $\gamma_t = 127.5 \times 2\pi$ MHz (255 MHz thermal linewidth) and $\gamma_{s.d.} = 500 \times 2\pi$ MHz (1 GHz spectral diffusion). The corresponding saturation Rabi frequency is $\Omega'_s = 11.4 \times 2\pi$ MHz.

Excited-state lifetime

We measure the excited-state lifetime of a micropuck-integrated T centre by pulsed resonant excitation. A single T centre resonance is identified on a 305-nm micropuck by PLE as shown in Fig. 2b. The excitation laser is then locked to this frequency and pulsed using an electro-optic amplitude modulator (EOM) (Jenoptik AM1310b) with 1 GHz bandwidth and an extinction ratio of 40 dB. The excitation laser is pulsed 2 µs on and 3 µs off with a measured optical rise/fall time of 10 ns. Photon arrival times are tagged using a IDQuantique ID900 time controller.

The transient fluorescence decay (shown in Extended Data Fig. 4) is well fit by an exponential with a time constant of $\tau = 802(7)$ ns, shorter by a factor of 1.17(1) than the 940 ns bulk homogeneous lifetime τ_H measured in ^{28}Si (ref. [36]). Purcell enhancement by the micropuck is one mechanism by which the excited-state lifetime may change. Extended Data Fig. 5a shows the Purcell factor P_f as a function of wavelength and micropuck radius for a single dipole at the micropuck centre oriented in the device plane, simulated using Lumerical FDTD. To find the total Purcell factor for a T centre we take a weighted average of this single-wavelength Purcell over the T spectrum. The total weighted Purcell is shown in Extended Data Fig. 5b. For a 305-nm micropuck, the Purcell factor expected at the micropuck centre is $P_f^w = 1.15$.

The lifetime changes according to

$$\frac{\tau}{\tau_H} = 1 + \eta_R(P_f^w - 1), \quad (8)$$

where η_R is the radiative efficiency and every radiative pathway has been included in the average P_f.

The measured lifetime change matches the simulation for unit radiative efficiency η_R but we cannot conclusively attribute the lifetime change to Purcell factor or reach strong conclusions about the radiative efficiency. The exact position and orientation of the centre remain unknown, and alternative explanations for the lifetime change exist. In particular, strain resulting from the SOI and micropuck interfaces may produce energy eigenstates comprising different momentum states, that is, mixing the TX_0 and TX_1 levels.

Four-level spin-optical Hamiltonian

We fit a four-level, semiclassical atom-light model to pump-probe measurements of the B field-split T PLE spectrum. For convenience of notation, we label the spin states ($g_H > g_E$): $|\downarrow_E\rangle, |\uparrow_E\rangle, |\downarrow_H\rangle, |\uparrow_H\rangle$, $|1\rangle, |2\rangle, |3\rangle, |4\rangle$. We solve the evolution of the reduced atomic density matrix $\hat{\rho}$ under excitation by either one or two classical fields according to the master equation[50]

$$\frac{\partial}{\partial t}\hat{\rho} = -\frac{i}{\hbar}[\hat{H}, \hat{\rho}] + \hat{\mathcal{L}}(\hat{\rho}). \tag{9}$$

We separate the Hamiltonian $\hat{H}$ into atomic ($\hat{H}_a$) and interaction ($\hat{H}_i$) components to work in the interaction picture. We further make the rotating wave approximation to reduce the electric dipole interaction Hamiltonian to

$$\hat{H}_i = -\frac{\hbar}{2}\sum_{i,j}\Omega_{ij}\hat{\sigma}_{ij} + \text{h.c.} \tag{10}$$

where $\sigma_{ij} = |i\rangle\langle j|$ is the atomic raising operator from state $|i\rangle$ to $|j\rangle$, $\Omega_{ij} = d_{ij} \cdot E_{ij}$ is the corresponding Rabi frequency, determined by the transition dipole moment d_{ij} and resonant electric field amplitude E_{ij}, and h.c. denotes the Hermitian conjugate. The atomic Hamiltonian is

$$\hat{H}_a = -\frac{\hbar}{2}\left(\Delta_1^L\hat{\sigma}_{11} + \Delta_2^L\hat{\sigma}_{22} + \sum_{i=1}^{4}\Delta_i^Z\hat{\sigma}_{ii}\right) \tag{11}$$

$$\Delta_i^Z = \frac{\mu_B|B_0|}{2}(\mp g_E \mp g_H), \tag{12}$$

where Δ_i^Z is the Zeeman splitting of level i (equation (1) in the main text) and Δ_i^L is the detuning of the laser addressing ground states $i = 1, 2$ from the zero-field transition energy. The non-unitary evolution of the system is captured through a Liouvillian superoperator containing all dissipative system dynamics. The Liouvillian has Lindblad form

$$\hat{\mathcal{L}} = \sum\frac{1}{2}\left(2\hat{C}\hat{\rho}\hat{C}^\dagger - \hat{C}^\dagger\hat{C}\hat{\rho} - \hat{\rho}\hat{C}^\dagger\hat{C}\right), \tag{13}$$

where Σ is a sum over the following collapse operators $\hat{C}$. Spontaneous decay (radiative or otherwise) is modelled with the atomic transition collapse operator $\hat{C}_{ij}^r = \sqrt{\Gamma_{ij}}\hat{\sigma}_{ij}$ where Γ_{ij} is the transition decay rate. Optical dephasing is included by adding extra collapse operators $\hat{C}_{ij}^d = \sqrt{\frac{\gamma}{2}}(\hat{\sigma}_{ii} - \hat{\sigma}_{jj})$ where γ is a constant dephasing rate and the low-power linewidth is $(\Gamma + 2\gamma)/(2\pi)$ GHz. For each of these operators $i = 3, 4$ and $j = 1, 2$.

We solve the master equation evolution using QuTiP, the quantum toolbox package for Python[51]. The fluorescence rate is modelled by the steady-state excited population $\langle\hat{\sigma}_{22}\rangle + \langle\hat{\sigma}_{33}\rangle$ of equation (9). The excited-state population data used for fitting are determined from the detected fluorescence by normalization to a saturated fluorescence value. The five pump-probe datasets in Fig. 3e are fit simultaneously with a single model. The excited-state decay rate and electron spin Landé factor are fixed to their bulk Si values[36], $\Gamma = 1/\tau_H = 169 \times 2\pi$ MHz and $g_E = 2.005$. This model does not account for lifetime changes induced by either Purcell or strain effects. Here γ is fixed to the thermal dephasing at rate at 4.3 K, $\gamma = 255/2 \times 2\pi = 127.5 \times 2\pi$ MHz.

Once again, spectral diffusion is incorporated by convolution by the normalized Gaussian spectral diffusion function $G(\Delta')$. We integrate over H_a numerically.

$$\hat{H}_a = -\frac{\hbar}{2}\int G(\Delta')((\Delta_1^L - \Delta')\hat{\sigma}_{11} + (\Delta_2^L - \Delta')\hat{\sigma}_{22})d\Delta' + \sum_{i=1}^{4}\Delta_i^Z\hat{\sigma}_{ii}. \tag{14}$$

The spectral diffusion HWHM γ_{sd}, B_0 and g_H are free fit parameters. We further define free fit parameters $\Omega_{p,r}$ for each of the probe and repump excitation laser powers (expressed as Rabi frequencies).

The transition Rabi frequencies Ω_{ij} and laser detunings $\Delta_{1,2}^L$ are determined separately for each pump-probe dataset according to the scan configuration. One of $\Delta_{1,2}^L$ is varied according to the probe scan range and the other is fixed at the pump value. Rabi frequencies $\Omega_{i,j}$ are set correspondingly to one of the laser powers Ω_p, Ω_r. depending on which laser is fixed and which is being scanned. The single-frequency PLE dataset is simulated similarly using a single field addressing both transitions B and C.

The transition decay rates $\Gamma_{i,j}$ are scaled by a free branching ratio parameter r that describes the relative dipole strength of the spin preserving transitions B, C to the spin changing transitions A, D.

$$\Gamma_{31} = \Gamma_{42} = \frac{r}{1+r}\Gamma \tag{15}$$

$$\Gamma_{41} = \Gamma_{3,2} = \frac{1}{1+r}\Gamma. \tag{16}$$

The transition Rabi frequencies are $\Omega_{i,j}$ scaled by r and also a free relative transition dipole/polarization overlap parameter p assuming that transitions A, D (B, C) have the same dipole orientation. We fit $r = 1.2(2)$ and $p = 2.9(3)$ along with the values given in the text.

With a free dephasing rate γ, the fit process returns $\gamma = 185(20) \times 2\pi$ (370 MHz FWHM), $\gamma_{s.d.} = 230(80) \times 2\pi$ MHz (460 MHz FWHM), $\Omega_p = 9(1) \times 2\pi$ MHz, $\Omega_r = 11(1) \times 2\pi$ MHz, $r = 1.6(2)$, $p = 2.6(2)$. This indicates a temperature of 4.7 K, which is slightly above the 4.3(3) K uncertainty range of our TX_0/TX_1 PL ratio temperature estimate. It is possible that any given centre has more or less dephasing than this model accounts for because of strain induced shifts of the TX_0 and TX_1 levels. The dephasing rate at a given temperature changes inversely with the TX_0–TX_1 splitting. The free fit compensates for this increased dephasing rate by decreasing the spectral diffusion to 460 MHz, close to the lower bound of what we have observed so far. In practice, this exchanges a Gaussian linewidth contribution for a Lorentzian linewidth contribution, and may reflect that the spectral diffusion process is not strictly Gaussian.

Photon autocorrelation

We measure intensity autocorrelation in a Hanbury Brown–Twiss intensity correlator by splitting the sideband luminescence output of the confocal microscope between two SNSPDs with a 50:50 fibre-coupled beam splitter. The background count rate is measured with both lasers on, far detuned from the centre, and averaged over daily measurements taken while collecting correlation data. The presented measurements are collected under resonant two-colour excitation of the inner transitions B and C, and we measure antibunching distinctive of a single-photon field.

For this measurement we choose the brightest T centre we measured that also has resolved ZPL splitting at field to maximize the correlation signal, which scales as the square of the count rate. Extended Data Fig. 6a shows the raw correlation histogram before background subtraction. The raw correlation function shows distinct photon antibunching with an uncorrected $g^2(0) = C(0) = 0.55(4)$, more than 11 s.d. below $g^2(0) = 1$ and therefore inconsistent with a classical (coherent) optical field, but just shy of the typical single-photon witness threshold $g^2(0) \leq 0.5$. This threshold is the zero-delay correlation bound of multiphoton Fock states ($g_N^2(0) = 1 - 1/N$ for the N photon Fock state) and represents the maximum antibunching possible for two independent emitters. Multiphoton squeezed states can be arbitrarily antibunched, but this is typically neglected for single-photon witnesses with emitters that can be assumed to produce no squeezing.

Because in this experiment the background count rate is comparable to the detected fluorescence rate, it is essential to subtract the

background contribution to assess the true correlation function of the fluorescence field. The background-corrected $g^2(\tau)$ is calculated from the normalized coincidence rate $C(\tau)$, signal rate S and background rate B by accounting for failed coincidences (coincidences involving one or two background counts) according to ref. [52]

$$g^2(\tau) = (C(\tau) - (1-\rho^2))/\rho^2 \quad (17)$$

$$\rho = \frac{S}{S+B}. \quad (18)$$

The background-subtracted correlation function is included in the main text as Fig. 3e and also here as Extended Data Fig. 6b. From the zero-delay time bin the background-corrected $g^2(0)$ is 0.20(6), 5 s.d. below the two-emitter limit. This is slightly above the ideal single-photon field $g^2(0) = 0$ because of the bin size required for statistically significant numbers of counts at these low coincidence rates. From this measurement, we conclude this is fluorescence from a single optical transition and the emitter is a single centre, as expected from the spectral and magnetic field behaviour. Because we simultaneously measure a ZPL splitting for the same centre, we can be confident that this is a measurement of a single isolated spin in silicon.

The temporal shape of the autocorrelation function contains further information about the emitter photodynamics. In this case, the $g^2(\tau)$ antibunching dip is narrower than the optical lifetime, consistent with the saturation power regime due to the dominance of optical excitation over emission $\Omega > \Gamma$. We fit three variants of the optical Bloch model above and plot them alongside the background-corrected data in Extended Data Fig. 6b. The autocorrelation function is very slightly bunched $g^2(\tau) > 1$ at $\tau \cong 500$ ns. This dynamic is typical of emitters with competing rates, for example a three level Λ system with asymmetric Rabi frequencies from each ground state, and indeed a four-level model with symmetric Rabi frequencies $\Omega_{13} = \Omega_{24}$ (orange) fails to capture this behaviour. Fitting the same model with free Rabi frequencies (black) matches the data well, and requires a Rabi frequency asymmetry factor of 1.7 between the B and C transitions, which is within the experimental uncertainty of the imbalance over this multi-week g^2 measurement. This fit is included in the main text (Fig. 3e). Spin-free systems can have no such asymmetry and, in those cases, bunching behaviour indicates a competing decay pathway, for example non-radiative decay through a metastable state[53]. For completeness, we have included a modified five-level version of the four-level optical Bloch model with an extra metastable ground state (green). The excited states decay non-radiatively and symmetrically to this fifth level, which in turn decays symmetrically to the ground states. For this fit, we once again fix the optical Rabi frequencies to be equal and fit the non-radiative decay rate and metastable lifetime as free parameters. The radiative efficiency returned by this method is 0.91(1) and the metastable lifetime is 3.3(1) μs. In each of these numerical models the optical fields are assumed to be resonant with transitions B and C, and all remaining parameters are fixed to the fit values from the pump-probe spectra, Fig. 3c. Compared to the $g^2(0)$ calculated from the zero-delay time bin alone, the fits include every bin in the antibunching dip and return $g^2(0) = 0.1900(1)$, indicating a vanishingly small multi-emitter probability.

Optical pulse scheme

The spin T_1 pulse sequence is realized by independently pulsing two Nanoplus lasers with fibre-coupled EOMs from Jenoptik. Pulse sequences are generated by the IDQ ID900 time controller. EOM biases are adjusted dynamically by EOM controllers (Thorlabs MX10A) every 2 min of the experiment cycle to reduce drift and maximize optical pulse extinction. Characterizing the optical pulses with SNSPDs reveals 10 ns optical rise/fall times and typical optical extinctions of 30 and 28 dB for each channel.

The spin transient is the measured luminescence difference between 'read' pulses (pulses one and three) and 'prepare' pulses (two and four). Because the B and C transitions are not perfectly resolved, some luminescence accompanies even the zero-delay prepare pulses. Normalizing the transient to the prepare pulse luminescence accounts for variations in excitation and collection efficiency with time. Pulse sequences with large t_{wait} take many hours to measure. For analysis, the transient ratios are further normalized to a reference pulse sequence with $t_{wait} = 2$ μs taken twice daily.

Data availability

Data are available on request. Correspondence and requests for materials should be addressed to S.S.

49. Irion, E., Burger, N., Thonke, K. & Sauer, R. The defect luminescence spectrum at 0.9351 eV in carbon-doped heat-treated or irradiated silicon. *J. Phys. C: Solid State Phys.* **18**, 5069–5082 (1985).
50. Lambropoulos, P. & Petrosyan, D. *Fundamentals of Quantum Optics and Quantum Information* (Springer, 2007).
51. Johansson, J. R., Nation, P. D. & Nori, F. QuTiP: an open-source Python framework for the dynamics of open quantum systems. *Comput. Phys. Commun.* **183**, 1760–1772 (2012).
52. Beveratos, A. et al. Room temperature stable single-photon source. *Euro. Phys. J. D. Atom. Mol. Opt. Plasma Phys.* **18**, 191–196 (2002).
53. Kitson, S. C., Jonsson, P., Rarity, J. G. & Tapster, P. R. Intensity fluctuation spectroscopy of small numbers of dye molecules in a microcavity. *Phys. Rev. A.* **58**, 620 (1998).

Acknowledgements We thank C. Clément from Polytechnique Montréal for rapid thermal annealing of implanted samples. This work made use of the 4D LABS and Silicon Quantum Leap facilities supported by the Canada Foundation for Innovation, the British Columbia Knowledge Development Fund, Western Economic Diversification Canada and Simon Fraser University. This work was supported by the Canada Research Chairs program, the New Frontiers in Research Fund: Exploration, the Canadian Institute for Advanced Research Quantum Information Science program and Catalyst Fund, Le Fonds de recherche du Québec: Nature et technologies and the Natural Sciences and Engineering Research Council of Canada.

Author contributions A.T.K.K., D.B.H. and S.S. designed the experiment and wrote the manuscript. A.T.K.K. and D.B.H. built the apparatus, measured single-centre spectra and analysed the data. M.K. and D.B.H. measured single spin lifetimes. N.A.B., A.T.K.K. and D.B.H. measured photon correlations. C.C., D.B.H., E.R.M. and S.R. developed the samples used in the study. J.R.K., N.R.L-H., J.S., M.R. and K.J.M. assisted in experiment design. C.B., L.B., A.D., N.A.B., S.R.H., J.K., M.K., D.W.M., T.S.R. and L.A.S. contributed to code development. M.L.W.T. advised on design and analysis. All authors participated in manuscript revision.

Competing interests D.B.H., A.T.K.K., C.C., M.K., N.A.B., E.R.M., N.R.L-H., M.R., C.B., L.B., J.K., L.A.S., K.J.M., M.L.W.T. and S.S. are current or recent employees of and/or have a financial interest in Photonic Inc., a quantum technology company. J.R.K., J.S., S.R.H., D.W.M., T.S.R. and S.R. declare no competing interests.

Additional information

Supplementary information The online version contains supplementary material available at https://doi.org/10.1038/s41586-022-04821-y.

Correspondence and requests for materials should be addressed to Stephanie Simmons.

Peer review information *Nature* thanks the anonymous reviewers for their contribution to the peer review of this work.

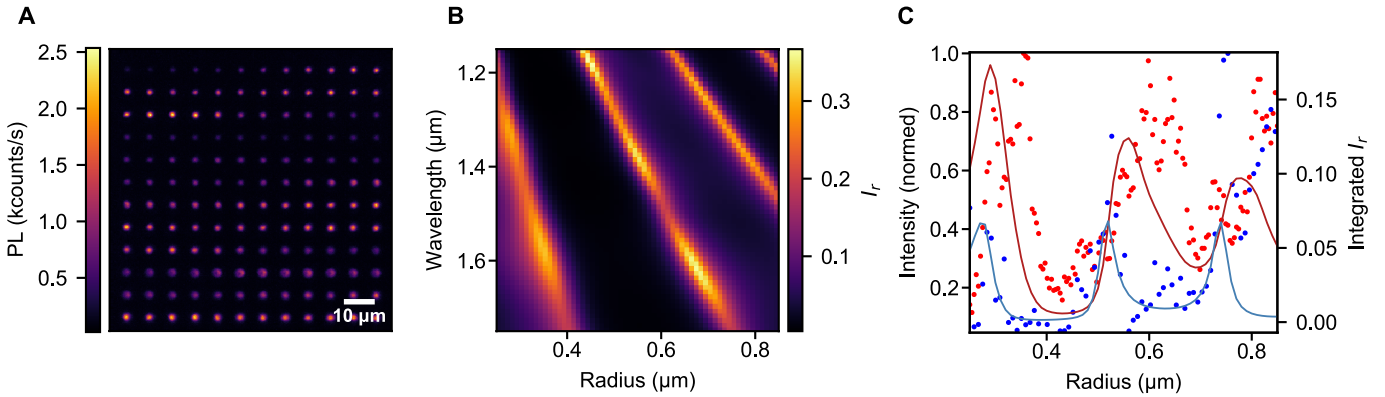

Extended Data Fig. 1 | Confocal microscopy of micropucks. (**A**) Confocal microscope image of micropucks, incrementing in radius from 250 nm (upper left) to 850 nm (bottom right), by integrating PL signal over $\lambda > 1.33$. (**B**) Simulated relative intensity (colour axis) collected by an NA = 0.7 microscope objective from a planar emitter at the micropuck centre as a function of wavelength and micropuck radius. (**C**) Simulated (solid) vs measured (dots) intensity of the T ZPL area (blue) and the integrated sideband intensity (red) in PL as a function of micropuck radius. Simulated data is plotted as relative intensity into the objective (right axis) and measured data is peak value normalized (left axis).

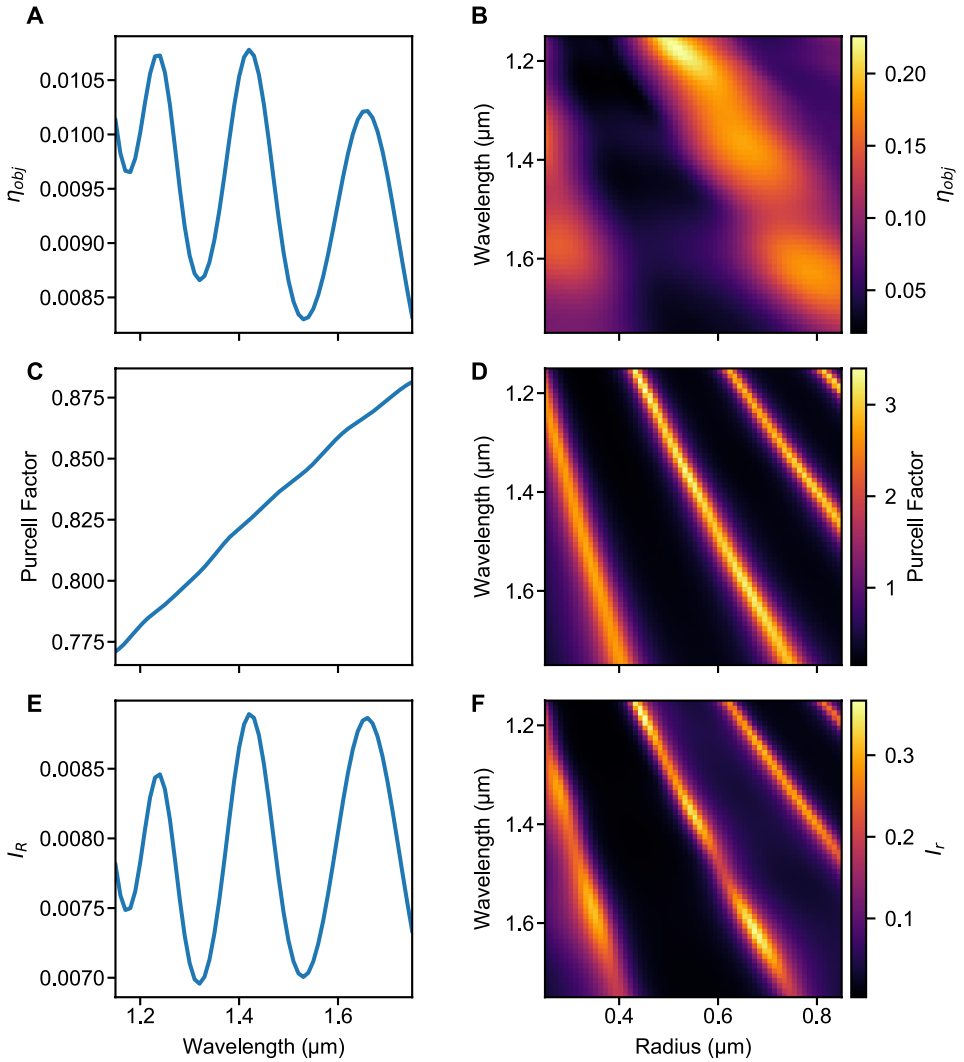

Extended Data Fig. 2 | FDTD simulated emission from micropucks. Collection efficiency (**A** and **B**), Purcell factor (**C** and **D**) and relative intensity (**E** and **F**) for a planar dipole in SOI (left column) and in a micropuck of varying radius (right column).

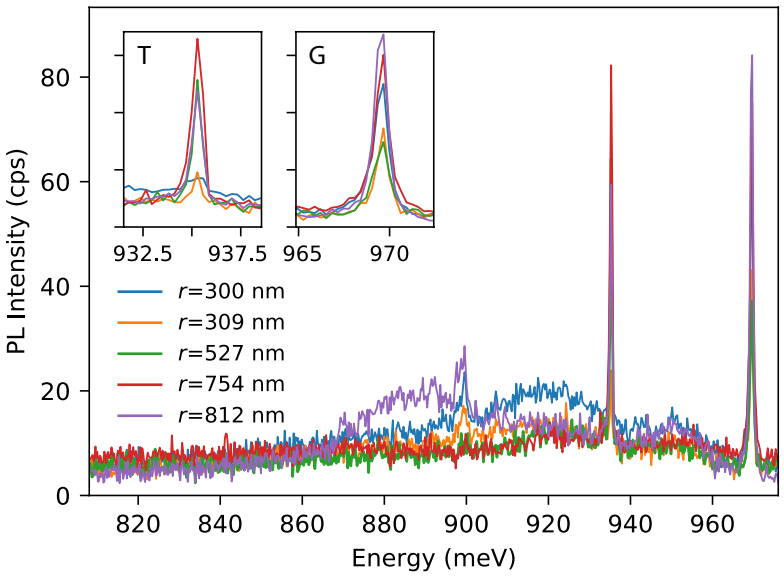

Extended Data Fig. 3 | Single micropuck PL spectra. The radius of each micropuck is given. Insets show zooms about the T and G centre ZPLs.

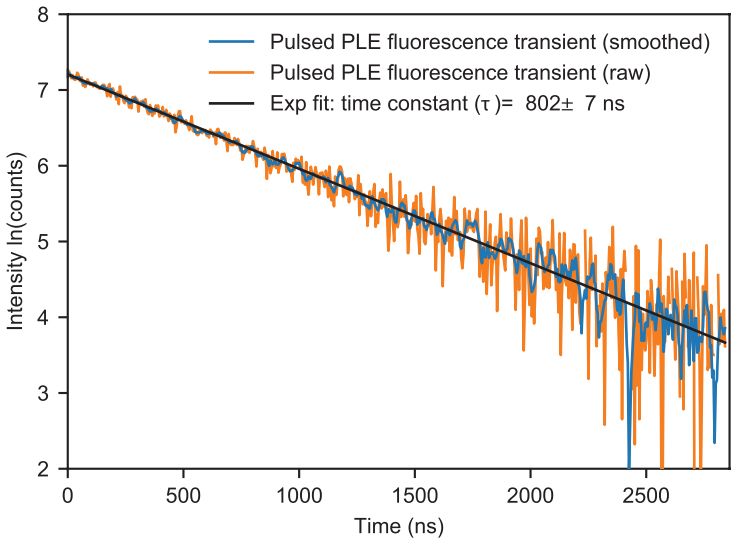

Extended Data Fig. 4 | Single T centre excited state lifetime. Fluorescence transient measured after resonant excitation. An exponential fit gives a lifetime of 802(7) ns.

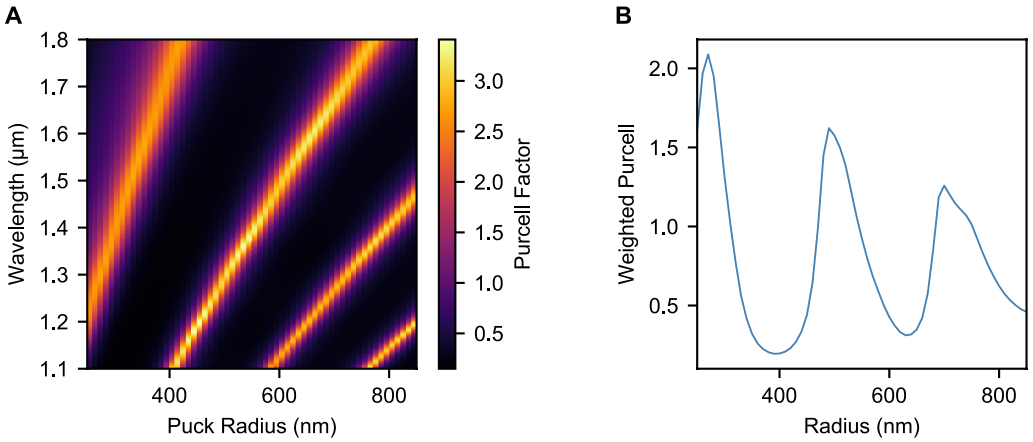

Extended Data Fig. 5 | FDTD simulated, spectrally weighted Purcell factor of a T centre in a micropuck. (**A**) Single-wavelength Purcell factor for a planar dipole at the centre of a micropuck of varying radius, reproduced from Extended Data Fig. 2(D) for reference. (**B**) Purcell factor averaged over the *T* centre spectrum as a function of micropuck radius.

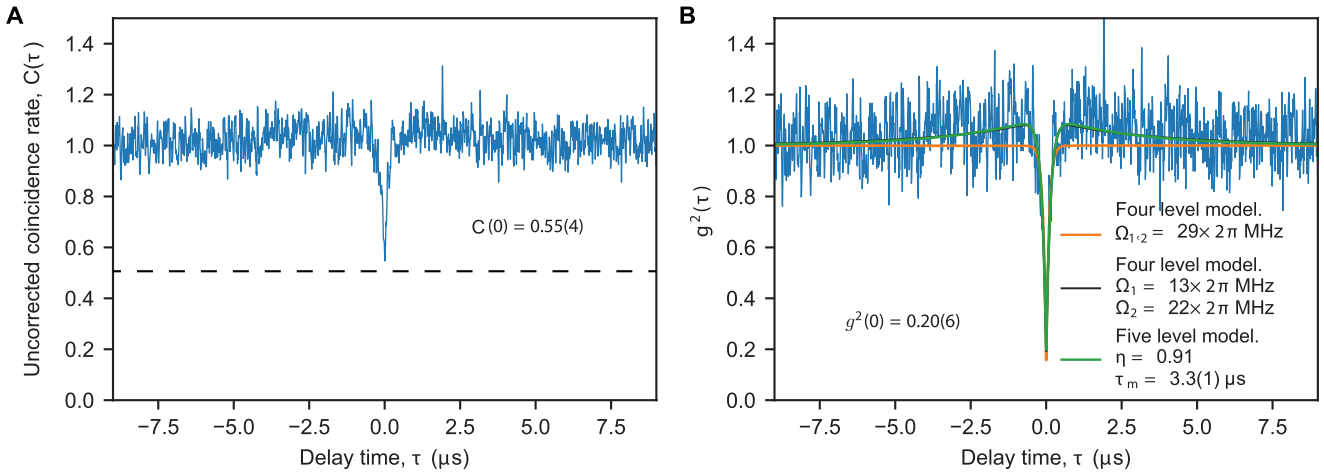

Extended Data Fig. 6 | Sideband fluorescence autocorrelation measurements. (A) Raw correlation histogram without background subtraction, normalized to the detection rate. (B) Background-subtracted correlation histogram with three fitted models.

Extended Data Table 1 | Summary of simulated relative intensities

Relative intensity	Range	Value
ZPL, I_r^{ZPL}	1.326	0.021
PSB (PL detection), I_r^{PSB}	1.33–1.60 μm	0.153
PLE detection, I_r^{PLE}	1.35–1.60 μm	0.146
Two-colour PLE detection, I_r^{TC}	1.40–1.60 μm	0.104
Full spectrum, I_r^{T}	1.32–1.60 μm	0.174

Extended Data Table 2 | Summary of measured losses

Source	Known	Value
APD, η_{D1}	spec.	0.15
SNSPD, η_{D2}	spec.	0.70
Detection path, η_{P}	meas.	0.33
Cryostat window transmission, η_{W}	meas.	0.66